

Air Force Institute of Technology

AFIT Scholar

Faculty Publications

3-2018


Influence of Basis-set Size on the $X^2\Sigma^+_{1/2}$, $A^2\Pi_{1/2}$, $A^2\Pi_{3/2}$, and $B^2\Sigma_{1/2}$ potential-energy curves, $A^2\Pi_{3/2}$ 2 vibrational energies, and D_1 and D_2 line shapes of Rb+He

L. Aaron Blank
Wright State University

Amit R. Sharma
Wright State University

David E. Weeks
Air Force Institute of Technology

Follow this and additional works at: <https://scholar.afit.edu/facpub>

 Part of the [Atomic, Molecular and Optical Physics Commons](#)

Recommended Citation

Blank, L. A., Sharma, A. R., & Weeks, D. E. (2018). Influence of basis-set size on the $X \Sigma_{1/2}^+ 2$, $A \Pi_{1/2} 2$, $A \Pi_{3/2} 2$, and $B \Sigma_{1/2}^+ 2$ potential-energy curves, $A \Pi_{3/2} 2$ vibrational energies, and D_1 and D_2 line shapes of Rb+He. *Physical Review A*, 97(3), 032705 (8 pp.). <https://doi.org/10.1103/PhysRevA.97.032705>

This Article is brought to you for free and open access by AFIT Scholar. It has been accepted for inclusion in Faculty Publications by an authorized administrator of AFIT Scholar. For more information, please contact AFIT.ENWL.Repository@us.af.mil.

Influence of basis-set size on the $X^2\Sigma_{1/2}^+$, $A^2\Pi_{1/2}$, $A^2\Pi_{3/2}$, and $B^2\Sigma_{1/2}^+$ potential-energy curves, $A^2\Pi_{3/2}$ vibrational energies, and D_1 and D_2 line shapes of Rb+He

L. Aaron Blank* and Amit R. Sharma†

Department of Physics, Wright State University, 3640 Colonel Glenn Highway, Dayton, Ohio 45435, USA

David E. Weeks

Department of Engineering Physics, Air Force Institute of Technology, 2950 Hobson Way, Wright-Patterson AFB, Ohio 45433-7765, USA



(Received 2 January 2018; published 22 March 2018)

The $X^2\Sigma_{1/2}^+$, $A^2\Pi_{1/2}$, $A^2\Pi_{3/2}$, and $B^2\Sigma_{1/2}^+$ potential-energy curves for Rb+He are computed at the spin-orbit multireference configuration interaction level of theory using a hierarchy of Gaussian basis sets at the double-zeta (DZ), triple-zeta (TZ), and quadruple-zeta (QZ) levels of valence quality. Counterpoise and Davidson-Silver corrections are employed to remove basis-set superposition error and ameliorate size-consistency error. An extrapolation is performed to obtain a final set of potential-energy curves in the complete basis-set (CBS) limit. This yields four sets of systematically improved $X^2\Sigma_{1/2}^+$, $A^2\Pi_{1/2}$, $A^2\Pi_{3/2}$, and $B^2\Sigma_{1/2}^+$ potential-energy curves that are used to compute the $A^2\Pi_{3/2}$ bound vibrational energies, the position of the D_2 blue satellite peak, and the D_1 and D_2 pressure broadening and shifting coefficients, at the DZ, TZ, QZ, and CBS levels. Results are compared with previous calculations and experimental observation.

DOI: [10.1103/PhysRevA.97.032705](https://doi.org/10.1103/PhysRevA.97.032705)

I. INTRODUCTION

The invention of the optically pumped alkali laser (OPAL) [1–5] has led to renewed interest in the spectroscopy of small concentrations of alkali-metal atoms vaporized in a rare-gas buffer. OPALs are three-level systems where the alkali-metal atoms are pumped on the D_2 transition, then make a collisionally induced transition from the $^2P_{3/2}$ to the $^2P_{1/2}$ excited atomic states, and then lase on the D_1 transition. The buffer gas is used to pressure broaden the alkali D_2 line to match the pump bandwidth as well as facilitate the fine-structure transition. This has driven recent interest in pressure-broadened D_1 and D_2 line shapes [6–10] of alkali-metal atoms as well as fine-structure transition rates [11,12].

In a previous effort [13], we calculated the broadening and shifting coefficients as a function of temperature for a set of nine OPAL diatomic pairs, each comprising an alkali-metal atom perturbed with a noble-gas atom. These calculations are based on the line-shape theory of Anderson and Talman [14] that utilizes difference potentials (DPs) between the upper and lower potential-energy curves (PECs) of the alkali-metal noble-gas pair. The results demonstrated the sensitivity of the broadening and shifting coefficients to the form of the long-range DPs, and their insensitivity to the intermediate and short ranges of the DPs. While the core of the spectral line shape is dependent primarily on the long-range interaction potentials, the line wing and associated satellite features depend strongly on the intermediate- and short-range region of the DPs, as well as on the dipole transition moments (see Allard *et al.* [15]).

In this paper, we first compute a set of systematically improved $X^2\Sigma_{1/2}^+$, $A^2\Pi_{1/2}$, $A^2\Pi_{3/2}$, and $B^2\Sigma_{1/2}^+$ PECs for Rb+He at the spin-orbit multireference configuration interaction level of theory using a hierarchy of Gaussian basis sets at the double-zeta (DZ), triple-zeta (TZ), and quadruple-zeta (QZ) levels of valence quality. Counterpoise and Davidson-Silver corrections are employed to remove basis-set superposition error and correct for size-consistency error. An extrapolation is performed to obtain a final set of potential-energy curves in the complete basis-set (CBS) limit. These systematically improved PECs are then used together with the dipole autocorrelation theory of spectral line shape [15] to study the effect of the systematic improvement of the PECs on various features of the D_1 and D_2 line shapes of Rb+He.

The discussion is organized as follows. In Sec. II, we give the details of the construction of *ab initio*-based PECs for a hierarchy of basis sets and extrapolation scheme used for computing the PECs in the CBS limit. The characteristics of the PECs and difference potential are discussed in Sec. III, followed by $A^2\Pi_{3/2}$ vibrational levels and their comparison with experimentally measured levels. The satellite peak position prediction and its convergence with basis-set size is also presented in this section, followed by the computation of line broadening and shifting coefficients and the influence of basis-set size on its values. Concluding remarks and a summary are given in Sec. IV.

II. COMPUTATIONAL APPROACH

Working within the framework of the nonrelativistic Hamiltonian, an alkali-metal atom in its ground electronic state has one electron in the outer s orbital, resulting in a doublet- S (2S) ground state. The noble-gas atom's ground electronic configuration results in a singlet- S (1S) state due to lack of

*laaronblank@gmail.com

†Corresponding author: amit.sharma@wright.edu

unpaired electrons. The resulting Σ molecular state that arises from the alkali-metal atom plus noble-gas atom system is labeled by $X^2\Sigma$ and has A_1 symmetry in the C_{2v} point group of the molecular frame. The lowest electronic excitation of the s electron into p orbital in the alkali-metal atom results in a 2P electronic state. Combining this with the ground 1S state of the noble-gas atom results in a $B^2\Sigma$ electronic state with A_1 symmetry and two $A^2\Pi$ degenerate electronic molecular states, one with B_1 symmetry and the other with B_2 symmetry. When the spin-orbit correction is introduced in the Hamiltonian, the $X^2\Sigma$ and $B^2\Sigma$ molecular states become $X^2\Sigma_{1/2}^+$ and $B^2\Sigma_{1/2}^+$, respectively. The $A^2\Pi$ states cease to be degenerate and split into $A^2\Pi_{1/2}$ and $A^2\Pi_{3/2}$ spin-orbit states, with $A^2\Pi_{1/2}$ being the lower of the two. These are the four lowest molecular electronic spin-orbit states for the Rb+He diatomic system studied in this work.

The electronic wave function of Rb+He is first calculated with the multiconfiguration self-consistent field (MCSCF) approach [16,17]. The rubidium nucleus and core electrons are represented by a spin-orbit effective core potential (SOECP) [18], whereas the Rb atom's valance electrons and the He atom's electrons are treated explicitly. The orbitals for the MCSCF are chosen according to the complete active space (CAS) formulation in the C_{2v} point-group symmetry. In the ground-state asymptotic limit, the $4s$ and $4p$ orbitals of Rb and the $1s$ orbital of He are doubly occupied. These orbitals are optimized in the MCSCF calculation, but are left out of the active space. The active space is comprised of the singly occupied $5s$ and unoccupied $5p$ orbitals of Rb. This active space of one electron in four orbitals results in four molecular reference states (two of symmetry A_1 , one B_1 , and one B_2). The same active space is used to perform multireference configuration interaction singles and doubles (MRCISD) calculations [19–21] to capture the correlation energy. The effect of inclusion of the doubly occupied He $1s$ orbital in the active space does not result in any significant difference in the results presented here and therefore we report calculations with four active orbitals. Size-extensivity error of the correlation energy is corrected by the standard method of Davidson and Silver [22], and the relativistic corrections to the electronic states are computed using a *state-interacting* method. In this method, the full Hamiltonian is made up of the sum of the nonrelativistic electronic Hamiltonian and the spin-orbit Hamiltonian, $\hat{H}_{el} + \hat{H}_{SO}$. This Hamiltonian is expanded in a basis set of MRCISD wave functions (solutions for \hat{H}_{el}), where we replace the eigenvalues of \hat{H}_{el} with their Davidson corrected counterparts. The result is known as the spin-orbit (SO) matrix, and its diagonalization results in the relativistic corrected energies. The SOECP is employed in the calculation of the matrix elements.

We consider a hierarchy of segmented contracted basis sets ranging from double-zeta and triple-zeta to quadruple-zeta quality. For the helium atom, def2-svp, def2-tzvp, and def2-qzvpp basis sets of Weigend and Ahlrichs [23–26] are used. The “def2” basis sets are improved versions of Stuttgart-Bonn-Köln pseudopotentials, where “p” and “pp” refer to smaller and larger sets of polarization functions, respectively. The def2-svp basis set is effectively a double-zeta quality contracted basis set of type $(4s, 1p) \rightarrow [2s, 1p]$. The def2-tzvp basis set consists

of $[3s, 2p, 1d]$ basis functions, and includes an additional polarization function over its def2-tzvp counterpart ($[3s, 1p]$). The def2-qzvpp basis set, $(8s, 3p, 2d, 1f) \rightarrow [4s, 3p, 2d, 1f]$, is augmented with an f -type polarization function.

For the Rb atom, basis sets dhf-svp, dhf-tzvp, and dhf-qzvpp [23,27] with associated ECP28MDF effective core potential from Weigend [28] are used. The SOECP descriptor, ECP28MDF, indicates that 28 core electrons are replaced by the pseudopotential; “M” denotes that a neutral atom was used for generating the pseudopotential and “DF” is an abbreviation for “Dirac-Fock relativistic.” Such ECPs are sometimes referred to as the relativistic effective core potential, which states that the ECP parameters are based on atomic Dirac-Fock theory. The dhf basis sets are larger and improved over def2 Rb basis sets.

The def2-svp and dhf-svp basis sets are collectively labeled as “DZ” in the remainder of this paper. Similarly, calculations performed with the def2-tzvp and dhf-tzvp are labeled as “TZ,” and those with def2-qzvpp and dhf-qzvpp are labeled as “QZ.” The calculations of PECs and dipole transition moments have been performed with the MOLPRO electronic structure program package [29].

Basis-set error correction

Weakly interacting systems such as Rb+He can suffer from significant basis-set superposition error (BSSE). We correct for this using the counterpoise procedure originally developed by Boys and Bernardi [30]. In general, the counterpoise correction to the energy takes the following form [31]:

$$\delta^{CP}(R) = \sum_i^N e_i^{\text{self}} - e_i^{\text{full}}(R), \quad (1)$$

where R is the internuclear separation, N is the number of fragments in the system, e_i^{self} is the energy of the i th fragment in its own basis, and e_i^{full} is the energy of the i th fragment in the full basis set with all the other fragments containing ghost atoms.

All molecular states considered in this work correlate with the helium atom in its ground 1S_0 state, and, the Rb+He molecular ground state ($X^2\Sigma_{1/2}^+$) correlates with the rubidium atomic ground state; therefore, Eq. (1) can be written as

$$\delta_{X^2\Sigma_{1/2}^+}^{CP}(R) = \text{Rb}_{2S_{1/2}}^{\text{self}} - \text{Rb}_{2S_{1/2}}^{\text{full}}(R) + \text{He}_{1S_0}^{\text{self}} - \text{He}_{1S_0}^{\text{full}}(R), \quad (2)$$

where $\text{Rb}_{2S_{1/2}}^{\text{self}}$ is the energy of the rubidium atom in its ground $^2S_{1/2}$ atomic state and its own basis, and $\text{Rb}_{2S_{1/2}}^{\text{full}}(R)$ is the energy of the rubidium atom in the same ground state and in both its own basis and the basis of a ghost helium atom placed at a distance R away from the rubidium. The terms for the energies of the helium atom are analogous. A calculation of the BSSE correction to the energy for the excited $A^2\Pi_{1/2}$ molecular state involves the He atom in its ground 1S_0 state and the rubidium atom in its first excited $^2P_{1/2}$ state,

$$\delta_{A^2\Pi_{1/2}}^{CP}(R) = \text{Rb}_{2P_{1/2}}^{\text{self}} - \text{Rb}_{2P_{1/2}}^{\text{full}}(R) + \text{He}_{1S_0}^{\text{self}} - \text{He}_{1S_0}^{\text{full}}(R). \quad (3)$$

The $A^2\Pi_{3/2}$ and $B^2\Sigma_{1/2}^+$ molecular states both involve the rubidium atom in its $^2P_{3/2}$ excited state, and thus both have

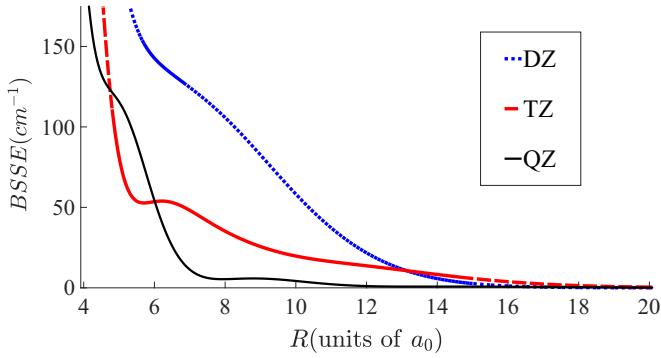


FIG. 1. BSSE in the $X^2\Sigma_{1/2}^+$ PECs calculated at the double-zeta (DZ), triple-zeta (TZ), quadruple-zeta (QZ) basis-set levels.

the same counterpoise correction to the energy,

$$\delta_{A^2\Pi_{3/2}}^{CP}(R) = \text{Rb}_{2P_{3/2}}^{\text{self}} - \text{Rb}_{2P_{3/2}}^{\text{full}}(R) + \text{He}_{1S_0}^{\text{self}} - \text{He}_{1S_0}^{\text{full}}(R), \quad (4)$$

$$\text{and } \delta_{B^2\Sigma_{1/2}^+}^{CP}(R) = \delta_{A^2\Pi_{3/2}}^{CP}(R).$$

The total BSSE correction to the $X^2\Sigma_{1/2}^+$ PEC for the DZ, TZ, and QZ basis sets as a function of R is shown in Fig. 1, where the size of the BSSE decreases as the valence quality of the basis increases. This trend in BSSE is caused by the more complete nature of the larger basis sets. It is interesting to note that the BSSE correction exhibited almost no difference when computed using Eqs. (2), (3), or (4) and as a result is essentially independent of the excitation level of the rubidium atom. This occurs because the excited-state wave functions are constructed using the same basis functions as the ground state. Thus, Eqs. (2)–(4) all yield the same values of the BSSE correction.

The calculated potential-energy surfaces (PES) are corrected for basis-set completeness by extrapolating the energy values to the complete basis-set limit using a mixed exponential and Gaussian approach of Peterson *et al.* [32],

$$E(X) = E_\infty + A \exp[-(X-1)] + B \exp[-(X-1)^2], \quad (5)$$

where X is the cardinality of the basis set (2 for DZ, 3 for TZ, etc.), $E(X)$ is the energy at a particular X , and, A , B , and E_∞ are fitting coefficients. The electronic structure energy at fixed internuclear distances is calculated using the DZ, TZ, and QZ quality basis including all of the corrections discussed above. The calculated energy values are then used to find the fitting coefficients in Eq. (5) using a least-squares approach. The coefficient E_∞ yields the extrapolated energy.

III. RESULTS AND DISCUSSION

The $X^2\Sigma_{1/2}^+$, $A^2\Pi_{1/2}$, $A^2\Pi_{3/2}$, and $A^2\Sigma_{1/2}^+$ molecular states of Rb+He computed at MRCISD in the complete basis-set size limit (corrected for basis-set superposition errors) are shown in Fig. 2. In the asymptotic limit of the ground electronic state,

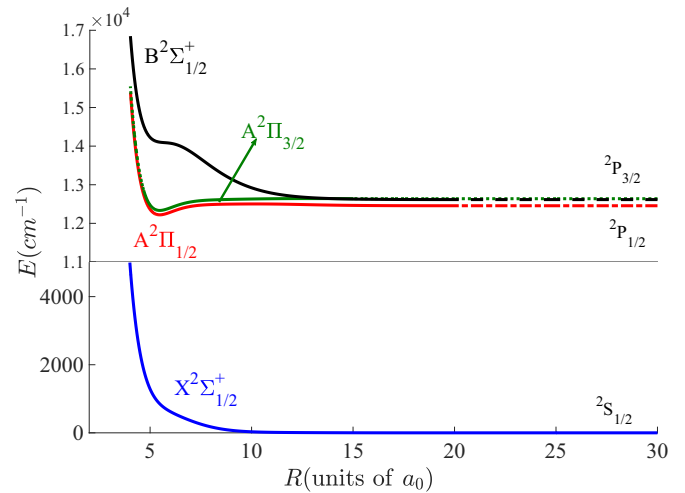


FIG. 2. The Rb+He molecular PECs calculated using multireference configuration interaction approach extrapolated to the complete basis-set limit from double zeta (DZ), triple zeta (TZ), and quadruple zeta (QZ) basis sets.

$X^2\Sigma_{1/2}^+$, the molecular energy corresponds to the sum of the ground $^2S_{1/2}$ atomic energy of Rb plus the ground 1S_0 atomic energy of He. As the internuclear distance (R) decreases, the $X^2\Sigma_{1/2}^+$ state is found to be repulsive with a negligible well of about 1 cm^{-1} , which is very sensitive to the level of theory used in computing the PECs. The asymptotic limit of the $A^2\Pi_{1/2}$ state of the molecular energy corresponds to the sum of the $^2P_{1/2}$ atomic energy of Rb and the ground 1S_0 atomic energy of He. As the internuclear separation decreases, a small barrier occurs before the $A^2\Pi_{1/2}$ state turns attractive, resulting in a potential well. In the asymptotic limit, the $A^2\Pi_{3/2}$ and the $B^2\Sigma_{1/2}^+$ PECs are degenerate and correspond to the $^2P_{3/2}$ atomic energy of Rb and the ground 1S_0 atomic energy of He. As the internuclear separation decreases, the molecular states diverge, with the $B^2\Sigma_{1/2}^+$ state becoming repulsive and the $A^2\Pi_{3/2}$ state becoming attractive. The repulsive nature of the $B^2\Sigma_{1/2}^+$ state exhibits a “shelf”-like feature around $R = 5\text{--}7 \text{ \AA}$. The $A^2\Pi_{3/2}$ state exhibits no barrier and its well is deeper than the $A^2\Pi_{1/2}$ well. Both of these wells’ equilibrium positions occur at the same value of R . A qualitative explanation of the nature of the nonrelativistic molecular electronic states has been outlined by Baylis [33]. In the $^2\Sigma$ state, the Rb electron is mainly in the spherically symmetric, σ molecular orbital, whereas in the $^2\Pi$ state, the alkali electronic wave function has π character with a node along the internuclear axis, allowing the He atom to approach the Rb atom closely before the repulsive interaction becomes dominant.

The shoulderlike structure observed on the $B^2\Sigma_{1/2}^+$ has been the subject of many investigations [34–37]. Pascale and Vandephanque [34] have shown that the $B^2\Sigma_{1/2}^+$ changes from a purely repulsive form (as calculated by Baylis [33]) and converges to a surface with shoulder when coupling of the $B^2\Sigma_{1/2}^+$ state with other neighboring states is included. The shoulder structure is also observed in the multichannel quantum defect theory (MQDT) potential surface calculations [35–37], wherein the atomic Hamiltonian consists of an ion

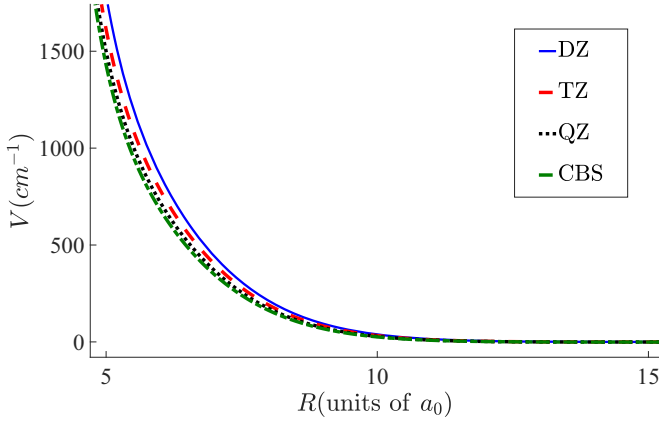


FIG. 3. The $X^2\Sigma_{1/2}^+$ PECs calculated at the DZ, TZ, QZ, and CBS basis-set levels.

core (Rb+) and a Rydberg electron and their interaction with the He atom. The excited electron experiences a pure Coulomb potential when the electron radial distance from the ion core is sufficiently large, allowing channel-mixing effects of the short-range interactions.

Figure 3 shows that the $X^2\Sigma_{1/2}^+$ of Rb+He becomes less repulsive as the basis-set size is increased. The $X^2\Sigma_{1/2}^+$ PEC exhibits a very shallow well of less than 1 cm^{-1} . A comparison of the well depth of the molecular ground state and its comparison with other theoretical estimates is presented in Table I. Previous studies [38] observed a significantly deeper well ($D_e \approx 10\text{ cm}^{-1}$) for the ground state for Rb+He, but those calculations did not correct the electronic structure calculation for BSSE. As seen in Table I, current values of r_{\min} are fairly close to earlier calculations and all agree to within 10% of each other. The dissociation energies exhibit a wider range of

TABLE I. Well depths D_e (cm^{-1}) and equilibrium positions r_{\min} (a_0) for the electronic energy states of Rb+He. We also include the barrier height and position for the $A^2\Pi_{1/2}$ state. We compare our results to other theoretical calculations. Note that the pseudopotential calculations by Pascale [39] and the density functional theory (DFT) calculations by Zbiri and Daul [40] report energies for the $A^2\Pi$ curve and are listed under both the $A^2\Pi_{1/2}$ and $A^2\Pi_{3/2}$ columns for ease of comparison.

Rb+He	$X^2\Sigma_{1/2}^+$	$A^2\Pi_{1/2}$		$A^2\Pi_{3/2}$
	Well	Well	Barrier	Well
D_e				
Current work	-0.9	-122.0	41.2	-188.4
Hirano <i>et al.</i> [41]		-102.1	26.5	-176.8
Zbiri and Daul [40]		-276		-276
Pascale [39]		-134		-134
Blank <i>et al.</i> [38]	-8.7	-95.9	20.0	-159.1
r_{\min}				
Current work	14.4	5.7	10.0	5.7
Hirano <i>et al.</i> [41]		6.1	10.0	6.1
Zbiri and Daul [40]		6.1		6.1
Pascale [39]		6.25		6.25
Blank <i>et al.</i> [38]	12.5	5.9	10.4	5.9

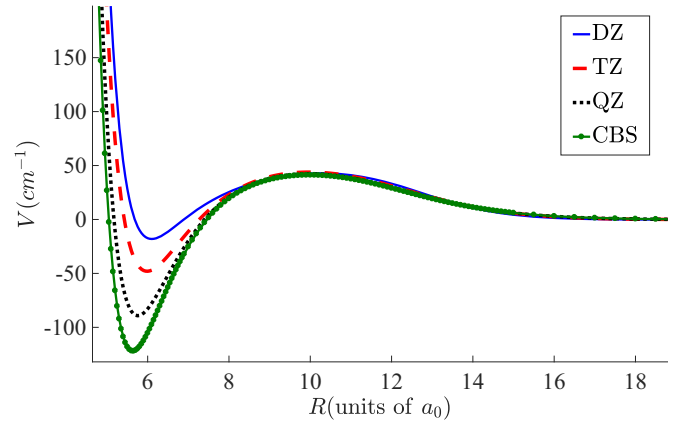


FIG. 4. The $A^2\Pi_{1/2}$ PECs calculated at the DZ, TZ, QZ, and CBS basis-set levels.

values and reflect the various methods and basis sets used for the calculations. Figures 4 and 5 show the convergence of the $A^2\Pi_{1/2}$ and $A^2\Pi_{3/2}$ states, respectively. The wells in both of these excited states strongly depend on the quality of the basis set. Increasing the basis-set size results in a deeper well, smaller equilibrium position, and lower anharmonicity. Note that the barrier in the $A^2\Pi_{1/2}$ state changes very little with increasing basis-set size. The convergence of the $B^2\Sigma_{1/2}^+$ PEC is shown in Fig. 6, where the shoulder becomes lower in energy and more pronounced as the basis set increases in size. It is interesting to note that the difference in energy between surfaces computed at the DZ and TZ levels in Figs. 4 and 5 is comparable to the difference in energy between surfaces computed at the TZ and QZ levels. This suggests that the basis-set extrapolation may not have completely converged and some improvement may be expected by performing the extrapolation using surfaces computed at the 5Z level.

The transition dipole moments of Rb+He are also calculated for a range of internuclear separation. The transition dipole moment for molecular states is assumed to be equal to that of the $\text{Rb } ^2P - ^2S$ transition in the asymptotic limit. Since these calculations are performed in C_{2v} point-group symmetry, the B_1-B_2 (transition between $^2\Pi$ states) transitions are forbidden, while the transition between all other states is allowed for a

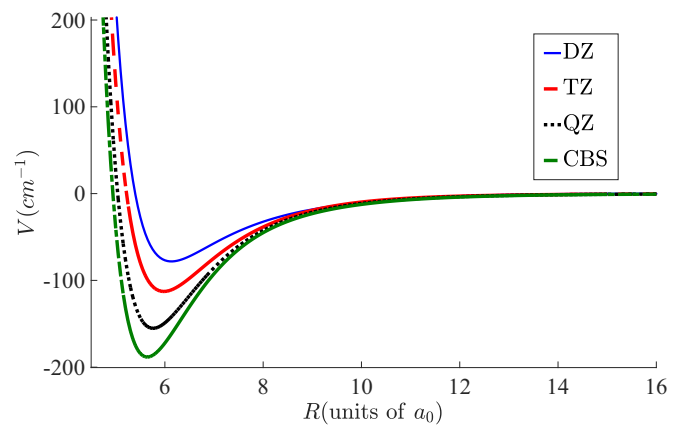


FIG. 5. The $A^2\Pi_{3/2}$ PECs calculated at the DZ, TZ, QZ, and CBS basis-set levels.

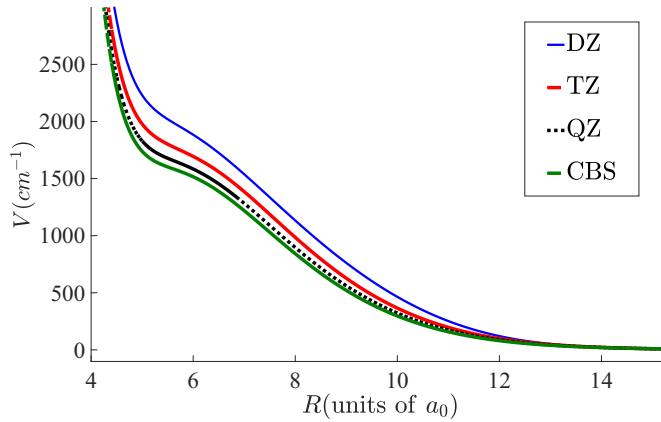


FIG. 6. The $B^2\Sigma_{1/2}^+$ PECs calculated at the DZ, TZ, QZ, and CBS basis-set levels.

certain component of the dipole moment. Transitions between states of the same symmetry A_1-A_1 (the $^2\Sigma$ ground and excited states) are possible for the z component of the dipole moment, which is parallel to the C_2 axis. Transitions between different symmetry states are possible for the x component of the dipole moment (A_1-B_1 ; the Σ ground state and one component of the $^2\Pi$ state) and for the y component of the dipole moment (A_1-B_2 ; $^2\Sigma$ states and B_2 component of the $^2\Pi$ state). It is observed that in the asymptotic limit (as expected), the transition moments $\langle ^2\Pi(B_1)|\mu_x|^2\Sigma(A_1)\rangle$, $\langle ^2\Pi(B_2)|\mu_y|^2\Sigma(A_1)\rangle$, and $\langle ^2\Sigma(A_1(2))|\mu_z|^2\Sigma(A_1(1))\rangle$ are equal in magnitude to the Rb $^2P - ^2S$ transition.

A difference of the order of about 6% is observed between transition moments calculated at the MCSCF level and MRCI level of theory. No significant difference is observed between transition moments at the MRCISD and spin-orbit configuration interaction (SOCI) levels; therefore only the MRCISD transition moment results are plotted in Fig. 7. The dipole transition moment between the $A^2\Pi_{1/2}$ state to the ground $X^2\Sigma_{1/2}^+$ state is the same as the dipole transition moment between the

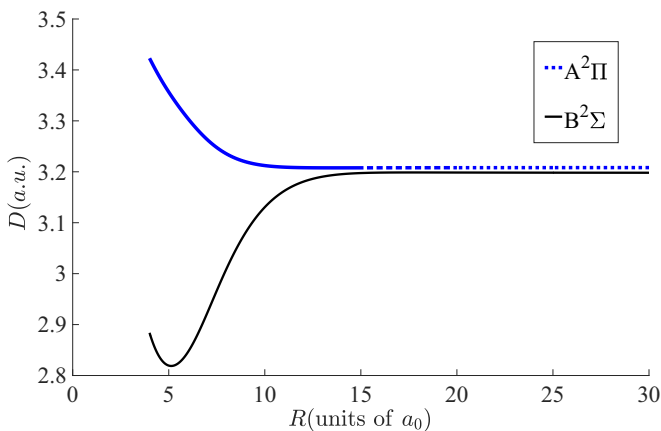


FIG. 7. Dipole transition moments between excited states and the ground state calculated at the MRCISD level of theory. The dipole moment labeled $A^2\Pi$ is applicable for either the $A^2\Pi_{1/2}$ or $A^2\Pi_{3/2}$ state as the choice of excited state. The dipole moment labeled $B^2\Sigma$ is appropriate for choosing the $B^2\Sigma_{1/2}^+$ state as the excited state.

TABLE II. Convergence for the Rb+He $A^2\Pi_{3/2}$ vibrational energy levels (in cm^{-1}).

E	DZ	TZ	QZ	CBS
E_0	27.7	34.2	42.7	49.0
E_1	61.7	82.2	105.2	122.2
E_2	76.1	107.7	140.2	165.3
E_3	78.6	112.8	153.8	184.2
E_4			155.8	188.6

$A^2\Pi_{3/2}$ and the ground state. In Fig. 7, we refer to this moment simply as $A^2\Pi$. The transition moment between the $B^2\Sigma_{1/2}^+$ and the ground state is referred to as $B^2\Sigma$. The dipole transition moments between all the excited states and the ground state show a small variation during the interaction. Such variations can effect the intensity of spectral line shapes induced by nonresonant collisions in the vicinity of the line wing [15].

Vibrational energy levels of the $A^2\Pi_{3/2}$ state are calculated by representing the nuclear Hamiltonian in a finite set of harmonic-oscillator basis functions and diagonalizing the resulting matrix [38]. The vibrational levels calculated for potential-energy surfaces with different basis sets are listed in Table II. We note that as the well depth increases in depth with increasing basis-set size, an additional vibrational state is observed from the TZ to QZ level of the basis set. In Table III, the vibrational energy-level difference is compared with experimental values and other theoretical calculations. It is interesting to note that in the present calculations, the $A^2\Pi_{3/2}$ well depth is larger compared to those calculated by Hirano *et al.*, but due to the difference in the shape of the PEC for $A^2\Pi_{3/2}$, we only observe five vibrational states compare to six as estimated by previous theoretical calculations. This can also be seen when comparing the difference between vibrational energy levels which are in very good agreement with experimentally measured levels, as shown in Fig. 8.

A. Satellite peak

The emission spectra of Rb+He is of great interest for optically pumped alkali laser (OPAL) applications. The D_2 line of rubidium when perturbed by helium has been observed to have a satellite peak at 735 nm [6]. The location of this peak can be predicted by collisional line-shape models operating in the quasistatic limit [14] using the equation for the intensity

TABLE III. Rb+He $A^2\Pi_{3/2}$ vibrational energy-level differences (in cm^{-1}) for $\Delta v = 1$ compared to experiment and two other theoretical calculations.

ΔE	This work	Expt. [42]	Theory [38]	Theory [41]
$E_1 - E_0$	73.2	65.8(3)	55.5	60.5
$E_2 - E_1$	43.1	43.7(2)	33.1	39.2
$E_3 - E_2$	19.0	23.2(7)	17.7	18.2
$E_4 - E_3$	4.4	8.8(6)	9.6	11.9
$E_5 - E_4$			4.5	7.9

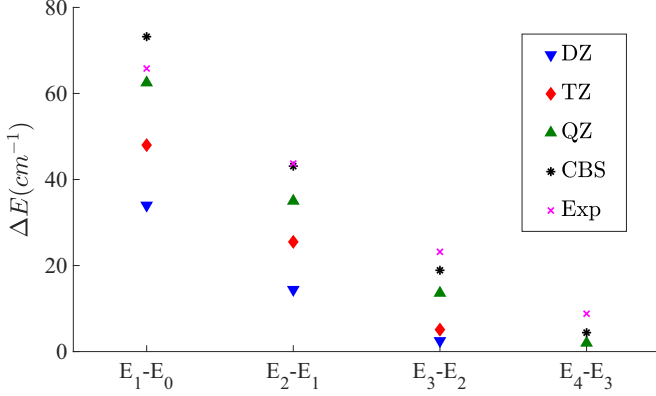


FIG. 8. Convergence of $A^2\Pi_{3/2}$ vibrational energy-level differences (in cm^{-1}) as a function of the basis set compared with known experimental values.

measured relative to the line center,

$$I(\omega) \propto \sum_c R_c^2 |D(R_c)|^2 \left| \frac{d(\Delta V)}{dR} \right|_{R_c}^{-1} \times n_{Ng} \exp \left[-\frac{X^2\Sigma_{1/2}^+(R_c)}{k_B T} \right], \quad (6)$$

where $D(R_c)$ is the transition dipole matrix element, n_{Ng} is the concentration of the noble gas, k_B is Boltzmann's constant, T is the absolute temperature, ΔV is the relevant difference potential (described below), $X^2\Sigma_{1/2}^+(R_c)$ is the ground-state PEC, and $R_c(\omega)$ are Condon points given by the solutions to the equation $\Delta V(R_c) = \hbar\omega$ [43]. Here it is assumed that the concentration of the rubidium gas is low relative to n_{He} , and the line broadening occurs only as a result of Rb+He collisions.

In order to use Eq. (6) to evaluate the satellite peak of the rubidium D_2 line, we must first identify the relevant difference potential. The D_2 line involves both the difference of the $A^2\Pi_{3/2}$ and $B^2\Sigma_{1/2}^+$ with the ground state since both of these excited states have asymptotic limits that correspond to the $^2P_{3/2}$ state of the rubidium atom [13]. However, it is only the difference potential from the $B^2\Sigma_{1/2}^+$ that influences the satellite peak position. This difference potential can be explicitly written as

$$\Delta V = [B^2\Sigma_{1/2}^+(R) - X^2\Sigma_{1/2}^+(R)] - \left[\lim_{R \rightarrow \infty} B^2\Sigma_{1/2}^+(R) - \lim_{R \rightarrow \infty} X^2\Sigma_{1/2}^+(R) \right]. \quad (7)$$

The difference potentials calculated by Eq. (7) at different levels of the basis set are presented in Fig. 9. It is primarily the shoulder of the $B^2\Sigma_{1/2}^+$ PEC discussed above which leads to the extremum depicted in Fig. 9. The lowering of the shoulder that occurs as the valence quality of the basis increases causes a corresponding reduction of the maximum energy of this extremum. The value of energy at which the extremum occurs corresponds directly to the frequency at which the satellite peak will appear. Table IV tabulates the results of these positions calculated at the DZ, TZ, QZ, and CBS levels and a systematic improvement in the predicted

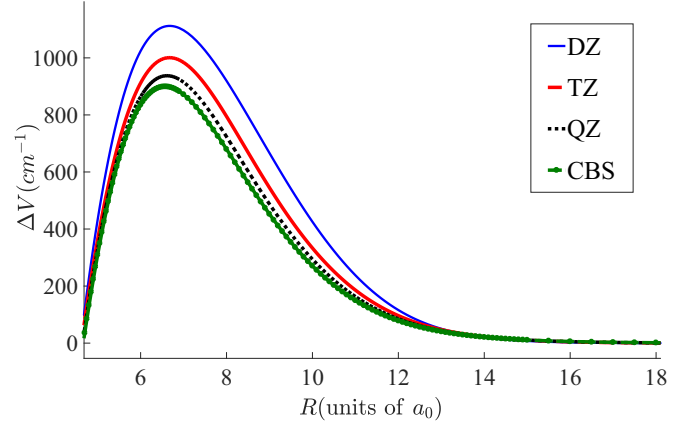


FIG. 9. The difference potential between the $B^2\Sigma_{1/2}^+$ and $X^2\Sigma_{1/2}^+$ PECs calculated at the double-zeta (DZ), triple-zeta (TZ), quadruple-zeta (QZ), and extrapolated (CBS) basis-set levels.

satellite line positions is observed. In regards to the satellite line position, preliminary calculations (not presented here) show that an all-electron basis set affects the $B^2\Sigma_{1/2}^+$ surface the most, over the internuclear separation range of 4–10 Bohr. The $B^2\Sigma_{1/2}^+$ surface is higher in energy (and altered shape) when compared with the PEC calculated with core potentials, resulting in a larger value of difference potential. This results in a blueshift of the satellite line position compared to the core potential predictions. A systematic study covering a hierarchy of all-electron basis sets followed by complete basis-set extrapolation is required to make any conclusive inferences about the effect of the core potential on the satellite line position predictions.

B. Broadening and shifting coefficients

The broadening and shifting coefficients of Rb perturbed by a buffer gas of He atoms have been calculated using difference potentials derived from the DZ, TZ, QZ, and CBS PECs, as described in the previous sections. We calculate the temperature-dependent coefficients using the Anderson-Talman (AT) theory of spectral line broadening [13] and present the results in Table V. We observe a systematic monotonic increase in line-broadening and line-shift predictions as a function of basis-set size. In the case of the D_1 line, this trend is explained by a close examination of the $A^2\Pi_{1/2} - X^2\Sigma_{1/2}^+$ DP in the asymptotic limit, as shown in Fig. 10. As the basis-set size is increased, the value of internuclear separation at which the DP reaches its asymptotic value moves to larger internuclear separation (moves outward). The broadening and shifting coefficients using AT theory can be expressed as the sum of an effective hard-sphere contribution and a long-range contribution, where the hard-sphere contribution is observed

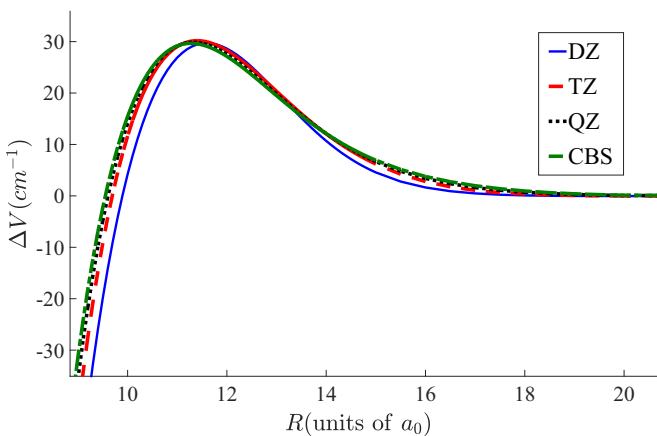
TABLE IV. Position (nm) of the satellite on the D_2 line of rubidium perturbed by helium.

	DZ	TZ	QZ	CBS	Expt. [6]
Satellite position	716	722	725	727	735

TABLE V. Pressure broadening and shift rates. In the table of rates below, the broadening (γ) and shift (δ) rates are given in $\text{cm}^{-1}/\text{cm}^{-3}$.

T(K)	Basis set	D_1		D_2	
		$\gamma (\times 10^{-20})$	$\delta (\times 10^{-21})$	$\gamma (\times 10^{-20})$	$\delta (\times 10^{-21})$
343	DZ	1.401	4.876	1.152	0.0832
	TZ	1.492	5.41	1.181	0.45
	QZ	1.53	6.02	1.198	0.90
	CBS	1.554	6.403	1.21	1.18
	Expt. [6]	0.954	5.45	1.01	0.24
394	DZ	1.460	5.496	1.22	0.0103
	TZ	1.558	6.104	1.252	0.050
	QZ	1.595	6.741	1.27	0.0965
	CBS	1.62	7.15	1.28	1.26
	Expt. [44]	1.29	6.41	1.36	0.504
	Theory [45]	1.07	-7.89	1.45	-1.54
Theory [13]	1.47	7.89	1.35	1.5	
450	DZ	1.51	6.11	1.29	0.124
	TZ	1.62	6.8	1.32	0.55
	QZ	1.65	7.46	1.34	1.03
	CBS	1.68	7.89	1.35	1.34
	Expt. [46]	1.33	6.42	0.972	2.74

to have a very small effect on shifting coefficients [13]. The hard-sphere contribution increases with basis-set size because the DP fall-off moves to larger internuclear separation and also the long-range contribution increases because the asymptotic energy value increases with the basis-set size. The net result of these contributions results in the monotonic trend observed in line broadening and line shift. The D_1 line broadening values at 343 K deviate from experimentally measured values by approximately 50–60% and the deviation is in the range of approximately 10–20% for 394 and 450 K. The D_1 line-broadening value at 394 K computed with the TZ basis set is within 6% of the previous theoretical estimate of Blank and Weeks [13], which is to be expected as the basis set used in their calculation was of similar TZ quality. The calculated D_1 line-shift values exhibit smaller deviation when compared


 FIG. 10. The difference potential between the $A^2\Pi_{1/2}^+$ and $X^2\Sigma_{1/2}^+$ PECs calculated at the double-zeta (DZ), triple-zeta (TZ), quadruple-zeta (QZ), and extrapolated (CBS) basis-set levels.

with experimentally measured values—underestimating for smaller basis set and overestimating in the CBS limit. The observation for the D_2 line is analogous, though it is more complicated because it depends on both the $A^2\Pi_{3/2} - X^2\Sigma_{1/2}^+$ and $B^2\Sigma_{1/2}^+ - X^2\Sigma_{1/2}^+$ DPs. Results in Table V are also compared with broadening and shifting coefficients computed using fully quantum-mechanical calculations that employ the Baranger theory of collisional line broadening.

IV. CONCLUSIONS

A hierarchy of segmented contracted basis sets at the DZ, TZ, and QZ levels of valence quality are used to compute the $X^2\Sigma_{1/2}^+$, $A^2\Pi_{1/2}$, $A^2\Pi_{3/2}$, and $B^2\Sigma_{1/2}^+$ potential-energy curves of Rb+He. The calculations are performed at the MRCISD level where the Rb nucleus and core electrons are represented by a SOECP [18] and the Rb atom's valence electrons and the He atom's electrons are treated explicitly. Basis-set superposition error is removed through a counterpoise correction, and size-consistency error is accommodated with a Davidson-Silver correction. Potential-energy curves computed at the DZ, TZ, and QZ levels are extrapolated to obtain $X^2\Sigma_{1/2}^+$, $A^2\Pi_{1/2}$, $A^2\Pi_{3/2}$, and $B^2\Sigma_{1/2}^+$ potential-energy curves in the CBS limit. The DZ, TZ, QZ, and CBS potential-energy curves are used to compute $A^2\Pi_{3/2}$ vibrational energies, the position of the D_2 satellite peak, and the broadening and shifting of the D_1 and D_2 lines. The potential-energy surfaces calculated in the present work are provided as Supplemental Material [47].

As expected, the size of the counterpoise correction to the potential-energy curves becomes smaller as the valence quality of the basis increases, with the primary effect of reducing the depth of the small $X^2\Sigma_{1/2}^+$ well at $R = 14.4(a_0)$ in the CBS limit. The effect of the counterpoise correction on the $A^2\Pi_{1/2}$ and $A^2\Pi_{3/2}$ wells is counterbalanced by an increase in well depth as the valence quality of the basis increases, and the difference between the $A^2\Pi_{3/2}$ vibrational energies converges toward the experimental result.

Since BSSE is nearly identical for the $X^2\Sigma_{1/2}^+$, $A^2\Pi_{1/2}$, $A^2\Pi_{3/2}$, and $B^2\Sigma_{1/2}^+$ potential-energy curves at all levels of valence quality, difference potentials used to compute line-shape features are not influenced by the counterpoise correction. On the other hand, line-shape features are strongly influenced by the valence quality of the basis used to compute the potential-energy curves and the corresponding difference potentials. For example, the shoulder on the $B^2\Sigma_{1/2}^+$ potential-energy curve is significantly lowered as the valence quality increases. This causes the maximum energy in the difference potential between the $B^2\Sigma_{1/2}^+$ and $X^2\Sigma_{1/2}^+$ potential-energy curves to correspondingly decrease. This maximum energy corresponds to the position of the blueshifted satellite peak and it follows that the D_2 satellite peak becomes less blueshifted and approaches the experimental value as the valence quality increases. As with the $A^2\Pi_{3/2}$ vibrational energy differences, the D_2 satellite peak is best predicted using the CBS potential-energy surface.

Anderson-Talman line-broadening theory is used together with difference potentials between the ground $X^2\Sigma_{1/2}^+$ potential-energy curve and the excited $A^2\Pi_{1/2}$, $A^2\Pi_{3/2}$, and $B^2\Sigma_{1/2}^+$ potential-energy curves to compute the broadening and

shifting coefficients of the D_1 and D_2 lines. As with the D_2 satellite peak, the counterpoise correction makes no contribution to the difference potentials and variations in broadening and shifting coefficients are determined by valence quality. As valence quality increases, the D_1 broadening coefficient diverges away from the experimental measurement, the D_1 shifting coefficient first approaches and then diverges from the experimental measurement, the D_2 shifting coefficient does appear to converge to the experimental measurement, and the D_2 shifting coefficient first approaches and then diverges from the experimental measurement. As noted in Ref. [13], both the broadening and shifting coefficients are highly sensitive to small changes in the asymptotic form of the difference potential and, as seen with these results, an accurate

calculation of line-shape coefficients remains a significant challenge.

ACKNOWLEDGMENTS

Generous support by the National Science Foundation (NSF) (MRI Award No. 1531923) is greatly appreciated (A.R.S.). The work is also supported in part by the U.S. Air Force Research Lab Summer Faculty Fellowship Program (A.R.S.). We are thankful to the NSF for the computational resources that were used for this research. A.R.S. would also like to acknowledge the funding provided by Wright State University.

-
- [1] W. Krupke, R. Beach, V. Kanz, and S. Payne, *Opt. Lett.* **28**, 2336 (2003).
- [2] R. J. Beach, W. F. Krupke, V. K. Kanz, and S. A. Payne, *J. Opt. Soc. Am. B* **21**, 2151 (2004).
- [3] B. V. Zhdanov, T. Ehrenreich, and R. J. Knize, *Opt. Commun.* **260**, 696 (2006).
- [4] R. H. Page, R. J. Beach, V. K. Kanz, and W. F. Krupke, *Opt. Lett.* **31**, 353 (2006).
- [5] B. V. Zhdanov, J. Sell, and R. J. Knize, *Electron. Lett.* **44**, 582 (2008).
- [6] W. S. Miller, C. A. Rice, G. D. Hager, M. D. Rotondaro, H. Berriche, and G. P. Perram, *J. Quantum Spectrosc. Radiat. Transfer* **184**, 118 (2016).
- [7] W. S. Miller, C. A. Rice, and G. P. Perram, *J. Quantum Spectrosc. Radiat. Transfer* **206**, 151 (2018).
- [8] G. A. Pitz, D. E. Wertepny, and G. P. Perram, *Phys. Rev. A* **80**, 062718 (2009).
- [9] G. A. Pitz, C. D. Fox, and G. P. Perram, *Phys. Rev. A* **82**, 042502 (2010).
- [10] G. D. Hager, G. E. Lott, A. J. Archibald, L. Blank, D. E. Weeks, and G. P. Perram, *J. Quantum Spectrosc. Radiat. Transfer* **147**, 261 (2014).
- [11] C. D. Lewis and D. E. Weeks, *J. Phys. Chem. A* **121**, 3340 (2017).
- [12] B. Eshel, J. A. Cardoza, D. E. Weeks, and G. P. Perram, *Phys. Rev. A* **95**, 042708 (2017).
- [13] L. Blank and D. E. Weeks, *Phys. Rev. A* **90**, 022510 (2014).
- [14] N. Allard and J. Kielkopf, *Rev. Mod. Phys.* **54**, 1103 (1982).
- [15] N. F. Allard, A. Royer, J. F. Kielkopf, and N. Feautrier, *Phys. Rev. A* **60**, 1021 (1999).
- [16] H.-J. Werner and P. J. Knowles, *J. Chem. Phys.* **82**, 5053 (1985).
- [17] P. J. Knowles and H.-J. Werner, *Chem. Phys. Lett.* **115**, 259 (1985).
- [18] I. S. Lim, P. Schwerdtfeger, B. Metz, and H. Stoll, *J. Chem. Phys.* **122**, 104103 (2005).
- [19] P. J. Knowles and H.-J. Werner, *Chem. Phys. Lett.* **145**, 514 (1988).
- [20] H.-J. Werner and P. J. Knowles, *J. Chem. Phys.* **89**, 5803 (1988).
- [21] P. J. Knowles and H.-J. Werner, *Theor. Chim. Acta* **84**, 95 (1992).
- [22] E. R. Davidson and D. W. Silver, *Chem. Phys. Lett.* **52**, 403 (1977).
- [23] F. Weigend and R. Ahlrichs, *Phys. Chem. Chem. Phys.* **7**, 3297 (2005).
- [24] A. Schaefer, H. Horn, and R. Ahlrichs, *J. Chem. Phys.* **97**, 2571 (1992).
- [25] A. Schaefer, C. Huber, and R. Ahlrichs, *J. Chem. Phys.* **100**, 5829 (1994).
- [26] F. Weigend, F. Furche, and R. Ahlrichs, *J. Chem. Phys.* **119**, 12753 (2003).
- [27] T. Leininger, A. Nicklass, W. Kuechle, H. Stoll, M. Dolg, and A. Bergner, *Chem. Phys. Lett.* **255**, 274 (1996).
- [28] F. Weigend and A. Baldes, *J. Chem. Phys.* **133**, 174102 (2010).
- [29] H.-J. Werner, P. J. Knowles, G. Knizia, F. R. Manby, and M. Schütz, *WIREs Comput Mol Sci* **2**, 242 (2012).
- [30] S. F. Boys and F. Bernardi, *Mol. Phys.* **19**, 553 (1970).
- [31] D. Asturiol, M. Duran, and P. Salvador, *J. Chem. Phys.* **128**, 144108 (2008).
- [32] K. A. Peterson, D. E. Woon, and T. H. Dunning Jr., *J. Chem. Phys.* **100**, 7410 (1994).
- [33] W. E. Baylis, *J. Chem. Phys.* **51**, 2665 (1969).
- [34] J. Pascale and J. Vandeplanque, *J. Chem. Phys.* **60**, 2278 (1974).
- [35] N. Y. Du and C. H. Greene, *J. Chem. Phys.* **90**, 6347 (1989).
- [36] E. de Prunelé, *Phys. Rev. A* **36**, 3015 (1987).
- [37] N. Y. Du, Ph.D. thesis, Louisiana State University, 1989.
- [38] L. Blank, G. S. Kedziora, and D. E. Weeks, *J. Chem. Phys.* **136**, 124315 (2012).
- [39] J. Pascale, *Phys. Rev. A* **28**, 632 (1983).
- [40] M. Zbiri and C. Daul, *J. Chem. Phys.* **121**, 11625 (2004).
- [41] K. Hirano, K. Enomoto, M. Kumakura, Y. Takahashi, and T. Yabuzaki, *Phys. Rev. A* **68**, 012722 (2003).
- [42] M. Mudrich, F. Stienkemeier, G. Droppelmann, P. Claas, and C. P. Schulz, *Phys. Rev. Lett.* **100**, 023401 (2008).
- [43] J. Szudy and W. Baylis, *Phys. Rep.* **266**, 127 (1996).
- [44] M. Rotondaro and G. Perram, *J. Quantum Spectrosc. Radiat. Transfer* **57**, 497 (1997).
- [45] R. D. Loper, Ph.D. thesis, Air Force Institute of Technology, 2013.
- [46] E. Roueff and A. Suzor, *J. Phys. France* **35**, 727 (1974).
- [47] See Supplemental Material at <http://link.aps.org/supplemental/10.1103/PhysRevA.97.032705> for Rb+He PECs computed at the DZ, TZ, QZ, and CBS level are available as supplementary material.